

Article

# Numerical Model of Supersaturated Total Dissolved Gas Dissipation in a Channel with Vegetation

Youquan Yuan <sup>1</sup>, Yinghan Huang <sup>2</sup>, Jingjie Feng <sup>1,\*</sup>, Ran Li <sup>1</sup>, Ruidong An <sup>1</sup> and Juping Huang <sup>1</sup>

<sup>1</sup> State Key Laboratory of Hydraulics and Mountain River Engineering, Sichuan University, Chengdu 610065, China; 2016223060059@stu.scu.edu.cn (Y.Y.); liran@scu.edu.cn (R.L.); anruidong@scu.edu.cn (R.A.); juping-huang@uiowa.edu (J.H.)

<sup>2</sup> Power China Zhongnan Engineering Corporation Limited, Changsha 410014, China; hyhscu@126.com

\* Correspondence: fengjingjie@scu.edu.cn; Tel.: +86-186-233-16161

Received: 8 October 2018; Accepted: 28 November 2018; Published: 1 December 2018



**Abstract:** The recent construction and operation of high dams have greatly changed the natural flood process. To meet the ecological demands and flood control requirements of rivers, dams discharge flow through the flood discharge facility, always accompanied by total dissolved gas (TDG) supersaturation in the water, which is harmful to fish. The purpose of this paper is to explore the dissipation characteristics and prediction methods of supersaturated TDG in water flowing through a floodplain covered with vegetation. A three-dimensional two-phase supersaturated TDG transportation and dissipation model considering the effects of vegetation was established. Using existing mechanism experimental results, the inner dissipation coefficient  $k_{in}$  of TDG in vegetation-affected flows was studied, and the quantitative relationships between the inner dissipation coefficient  $k_{in}$  and the average flow velocity, average water depth, average water radius, Reynolds number, and vegetation density were characterized. Based on the simulation results, the distribution characteristics of the supersaturated TDG in water around vegetation and in the vertical, lateral, and longitudinal directions of the flume under different flow and vegetation densities were analyzed. A supersaturated TDG transportation and dissipation model for vegetation-affected flow is proposed and can be used to predict the impact of TDG in a floodplain.

**Keywords:** total dissolved gas; supersaturation; vegetation; two-phase model; dissipation

## 1. Introduction

Flooding is an important source of sediment and nutrients to a variety of downstream riverine, estuarine, and marine environments, and plays a crucial role in the development of ecosystems and in geologic and geomorphologic changes [1–4]. With the large-scale exploitation of hydropower, terraced reservoirs have gradually formed on rivers to regulate flooding [5,6], consequently changing the natural flood process. To meet the ecological demands of fish with respect to typical flood processes, some projects are currently trying to create artificial floods by dam spillage. For example, the Three Gorges Dam has long produced artificial flood peaks that stimulate fish to spawn [7]. During the dam spillage period, the water level of the downstream river channel rises sharply, and part of the coastal floodplain becomes submerged, connecting the aquatic and terrestrial ecosystems [8,9]. Generally, floodplains are covered by vegetation. The resistance effect of vegetation slows down the flood flow rate, and the nutrients carried by floods settle in the floodplain along with the sediment, allowing floodplains to become an important place for fish to fatten [10]. However, during the high dam discharge, a large amount of gas is entrained into the plunge pool by the nappe flow and then dissolved into the deep water in the high-pressure environment, allowing the total dissolved gas (TDG) in the water to reach supersaturation [11]. The supersaturated TDG cannot be fully released

back to the atmosphere over a short period of time [12,13], which may lead to fish suffering from gas bubble disease (GDB) and even death [14,15]. Therefore, studying the dissipation characteristics of supersaturated TDG on a floodplain covered with vegetation is of great significance for better protecting fish and ecological environments in rivers.

Currently, researches on the dissipation process of supersaturated TDG focus on the dissipation mechanism of supersaturated TDG in rivers without the effect of vegetation and reservoirs or the influence of environmental factors on this process. Based on the results of mechanism experiments or numerical simulations, some scholars have discussed the factors affecting the dissipation of supersaturated TDG and the corresponding mitigation measures, finding that reducing the water depth, increasing the water temperature, increasing the wind speed above the water surface, and aerating the water [16–19] can accelerate the dissipation of supersaturated TDG. Shen et al. [20] simulated the supersaturated TDG distribution in the confluence of a river after construction of a down-stream dam or a water-blocking pile and no engineering measures and found that constructing engineering measures at the intersection of rivers could create an area with low TDG saturation for fish to temporarily avoid the adverse effects of supersaturated TDG. Witt et al. [21] developed an empirically derived time-variant cross correlation methodology to predict the TDG travel time between an upstream hydropower spillway and a downstream dam, finding that retention time was a key factor affecting TDG level. Yuan et al. [22] developed a series of experiments on the vegetation's effect on the dissipation of the supersaturated TDG and showed that the presence of vegetation in the still water could adsorb supersaturated TDG, thereby facilitating its dissipation. The wall's adsorption coefficient was proposed and was proven to be mainly affected by the vegetation's material properties at the same time. On the other hand, some scholars have carried out substantial model research on the dissipation of supersaturated TDG. Analyzing the field monitoring TDG data on the Columbia River and its tributary Snake River, University of Washington researchers concluded that the dissipation process of supersaturated TDG followed a first-order kinetic reaction and accordingly proposed a longitudinal one-dimensional constant flow prediction model. In this model, an important parameter, the dissipation coefficient, representing the dissipation rate of TDG, was introduced [23]. Combined with field observation data and mechanism experiment data, Feng et al. [12] proposed a formula for predicting the dissipation coefficient of supersaturated TDG, which involved the factors of friction velocity, the hydraulic radius, the water depth and the Froude number. Perkins and Richmond [24] established a depth-averaged two-dimensional model, MASS2, to simulate the TDG distribution in shallow rivers and to further estimate its impact on fish. Johnson et al. [25] adopted the model MASS2 to calculate the TDG concentration in the reaches downstream of the Bonneville Dam and the Ice Harbor Dam. Ma et al. [26] developed a one-dimensional unsteady TDG model to predict the transportation and dissipation of supersaturated TDG downstream of a high dam under different discharge patterns, demonstrating that the temporal duration of TDG levels in the downstream river, which was a major factor determining the negative effects of TDG on fish, increased with increasing discharge time. Therefore, a discontinuous discharge pattern, rather than a continuous one, was recommended. Witt et al. [27] proposed a reduced-order TDG uptake equation to predict tailrace TDG at seven hydropower facilities on the middle section of the Columbia River; according to this equation, it was possible to reduce TDG supersaturation and meet hydropower generation requirements by shifting spillway flows at different times. To estimate the distribution of TDG in a reservoir, Feng et al. [28] established a laterally averaged two-dimensional unsteady model that included the dissipation coefficient of the TDG and the mass transfer coefficient through the free surface.

As mentioned above, most studies on the dissipation process of supersaturated TDG only considered the air-water free interface mass transfer and gas-liquid interface mass transfer, thus ignoring the influence of vegetation. As we know, the hydrodynamics characteristics and sediment transport in vegetated channels are different from those in channels without vegetation [29,30]. When the high dam discharge results in flooding, the submerged vegetation on the coastal floodplain of the downstream river can change the distribution of river flow velocity, affect the development of

turbulent kinetic energy, and alter the kinetic energy correction coefficient and momentum correction coefficient [31–33]. At the same time, the presence of vegetation in flowing water can increase the resistance and the shear force of the riverbed, thus reducing the flooding-induced erosion of the riverbed [34–36]. The presence of vegetation can also significantly affect the transportation of sediment and dissolved substances in the flow [37–40]. Huang [41] found that the TDG saturation difference between upstream and downstream of a flume significantly increased after supersaturated TDG water flowed through a vegetated area. Some scholars have also built a large number of numerical models to study the flow characteristics under the influence of vegetation. Huai et al. [42] presented a three-layer analytical model for open channel flow through suspended rigid vegetation, which could provide a vertical profile of streamwise velocities. Yang et al. [43] developed a two-dimensional lattice Boltzmann model with a D2Q9 lattice arrangement to simulate the flow-vegetation interactions in an open channel. Beudin et al. [44] established a coupled wave-flow-vegetation module in the COAWST modeling system that reproduced key features of flow-vegetation hydrodynamic interactions, particularly the strong shear layer at the top of a submerged canopy that varied in height as the plants bent.

The existing achievements show that the absence of vegetation significantly affects the flow characteristics and flow conditions of rivers. Numerous results have been published regarding the flow characteristics of vegetated flow and the transportation behavior of sediment in vegetated flow. However, there are few intensive studies on the transportation characteristics of supersaturated TDG in vegetated flow. In addition, there is also a lack of mathematical models that reflect the vegetation wall adsorption effect on supersaturated TDG. Based on Huang's experimental research, this paper establishes a three-dimensional two-phase flow model to predict the transportation of supersaturated TDG in a vegetated flume and analyzes the dissipation properties of the supersaturated TDG in vegetated flow.

## 2. Materials and Methods

### 2.1. Study Case

Huang (2017) [41] designed a physical experiment to study the flow characteristics under different flow characteristics and vegetation densities and to assess the vegetation's promoting effect on the dissipation of supersaturated TDG. The experimental device is shown in Figure 1. The main body of the experimental device is a Plexiglas flume (50 cm in width, 1500 cm in length, and 30 cm in height, with a slope of 0.45‰). Vertical Plexiglas columns (with cross-sectional dimensions of 1 cm × 1 cm and a height of 20 cm) were used instead of rigid emergent plants. The flow velocity was measured with an LGY-2 intelligent current meter, with a measuring range of 1–300 cm·s<sup>-1</sup> and a measurement error of equal to or less than 1.5%. The TDG saturation level in the water was detected with a TGP (Total Dissolved Gas Pressure) detector composed of Point Four TGP portable trackers made by Pentair (Minnesota, USA), with a TGP measuring range of 0–200% and an accuracy of 2%.

There were five groups of vegetation density  $d_V$  (the percentage of the ratio between the projected area of vegetation in the Z direction and the area of the flume's bottom) and five groups of flow, resulting in a total of 25 experimental cases as shown in Table 1. Figure 2 shows the arrangement of the Plexiglas columns.

During a certain experimental process, the flow rate is constant and the flow in the flume is steady flow. In the absence of vegetation, the flow in the whole flume is non-uniform flow.

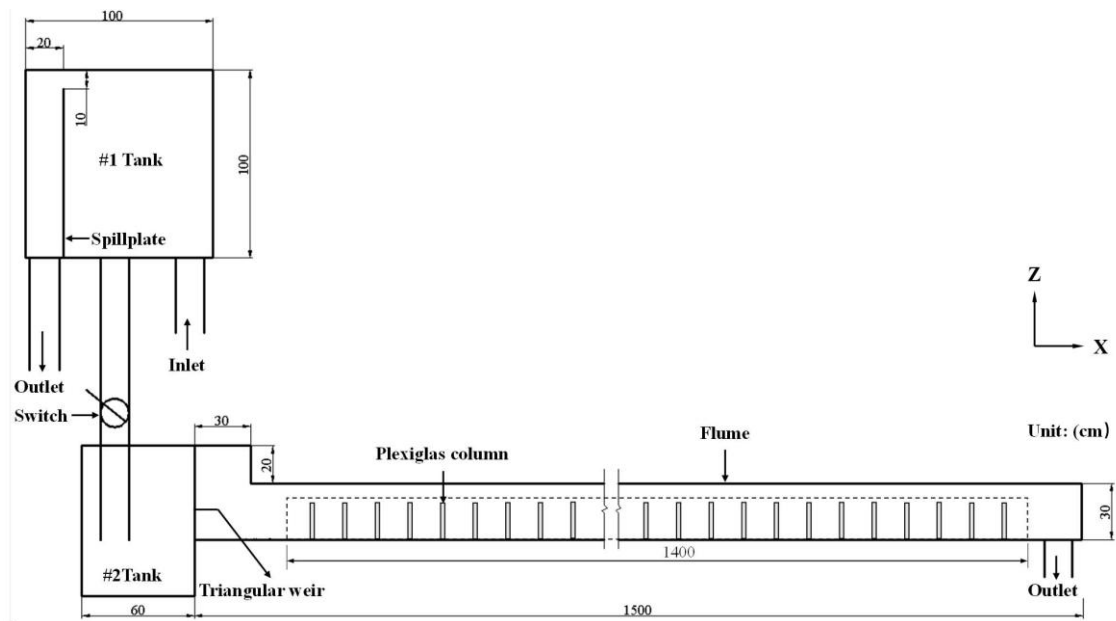


Figure 1. Sketch of the experimental devices.

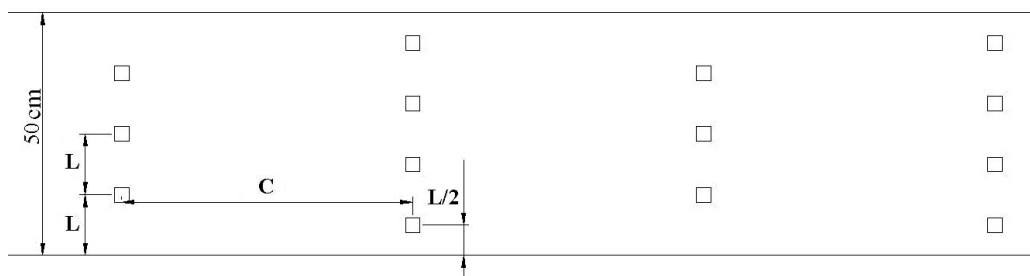


Figure 2. The arrangement of Plexiglas columns in the experimental flume.

Table 1. The conditions of experimental cases.

Case No.	Flow (L.s <sup>-1</sup> )	The Vegetation Density	Lateral Space L <sub>y</sub> (10 <sup>-2</sup> m)	Longitudinal Space L <sub>x</sub> (10 <sup>-2</sup> m)	The Flow Depth h (10 <sup>-2</sup> m)	TDG Saturation of Entry Section (%)
1	1.5	0	/	/	2.2	144.5
2	3.5	0	/	/	3.8	144.4
3	5.5	0	/	/	4.7	145.6
4	7.5	0	/	/	5.6	147.1
5	9.5	0	/	/	6.6	148.1
6	1.5	0.1	12.5	60	2.5	144.2
7	3.5	0.1	12.5	60	4.4	144.6
8	5.5	0.1	12.5	60	5.3	144.5
9	7.5	0.1	12.5	60	6.4	146.6
10	9.5	0.1	12.5	60	7.5	147.9
11	1.5	0.2	7.1	60	2.8	144.9
12	3.5	0.2	7.1	60	4.6	147.4
13	5.5	0.2	7.1	60	5.8	148.5
14	7.5	0.2	7.1	60	7.2	148.6
15	9.5	0.2	7.1	60	8.6	149.0
16	1.5	0.3	12.5	20	3.1	145.3
17	3.5	0.3	12.5	20	4.7	145.9
18	5.5	0.3	12.5	20	6.6	147.5
19	7.5	0.3	12.5	20	7.8	147.8
20	9.5	0.3	12.5	20	9.0	148.6
21	1.5	0.6	7.1	20	3.2	145.7
22	3.5	0.6	7.1	20	5.9	147.5
23	5.5	0.6	7.1	20	7.6	148.5
24	7.5	0.6	7.1	20	8.4	149.3
25	9.5	0.6	7.1	20	9.6	149.7

## 2.2. Model Assumption

Some scholars have considered the liquid–bubble interface mass transfer when simulating the generation, transportation, and dissipation of supersaturated TDG in water containing many bubbles, such as water in the plunge pool near a dam or in aerated water [45–47]. However, there are few bubbles in the channel downstream of a dam. Therefore, the effect of bubbles on the flow field is ignored in this model.

## 2.3. Model Equations

### 2.3.1. Continuity Equation

$$\frac{\partial \rho}{\partial t} + \frac{\partial}{\partial x}(\rho u) + \frac{\partial}{\partial y}(\rho v) + \frac{\partial}{\partial z}(\rho w) = 0 \quad (1)$$

$$\rho = \gamma \rho_w + (1 - \gamma) \rho_g \quad (2)$$

$$\frac{\partial \gamma}{\partial t} + \gamma \left( \frac{\partial u}{\partial x} + \frac{\partial v}{\partial y} + \frac{\partial w}{\partial z} \right) = 0 \quad (3)$$

where  $u$ ,  $v$  and  $w$  ( $\text{m}\cdot\text{s}^{-1}$ ) represent the flow velocities in the  $x$ ,  $y$ , and  $z$  directions, respectively;  $\rho$  ( $\text{kg}\cdot\text{m}^{-3}$ ) represents the density of the mixture of water and air;  $\rho_g$  ( $\text{kg}\cdot\text{m}^{-3}$ ) represents the density of air;  $\rho_w$  ( $\text{kg}\cdot\text{m}^{-3}$ ) represents the density of water;  $\gamma$  represents the volume fraction of water.

### 2.3.2. Momentum Equation

$$\begin{aligned} \frac{\partial \rho u}{\partial t} + \frac{\partial \rho u u}{\partial x} + \frac{\partial \rho u v}{\partial y} + \frac{\partial \rho u w}{\partial z} = -\frac{\partial p}{\partial x} + \frac{\partial}{\partial x} \left[ 2\mu \frac{\partial u}{\partial x} - \frac{2}{3} \left( \frac{\partial u}{\partial x} + \frac{\partial v}{\partial y} + \frac{\partial w}{\partial z} \right) \right] \\ + \mu \frac{\partial}{\partial y} \left( \frac{\partial u}{\partial y} + \frac{\partial v}{\partial x} \right) + \mu \frac{\partial}{\partial z} \left( \frac{\partial u}{\partial z} + \frac{\partial w}{\partial x} \right) + \rho f_x \end{aligned} \quad (4)$$

$$\begin{aligned} \frac{\partial \rho v}{\partial t} + \frac{\partial \rho v u}{\partial x} + \frac{\partial \rho v v}{\partial y} + \frac{\partial \rho v w}{\partial z} = -\frac{\partial p}{\partial y} + \frac{\partial}{\partial y} \left[ 2\mu \frac{\partial v}{\partial y} - \frac{2}{3} \left( \frac{\partial u}{\partial x} + \frac{\partial v}{\partial y} + \frac{\partial w}{\partial z} \right) \right] \\ + \mu \frac{\partial}{\partial z} \left( \frac{\partial v}{\partial z} + \frac{\partial w}{\partial y} \right) + \mu \frac{\partial}{\partial x} \left( \frac{\partial v}{\partial x} + \frac{\partial u}{\partial y} \right) + \rho f_y \end{aligned} \quad (5)$$

$$\begin{aligned} \frac{\partial \rho w}{\partial t} + \frac{\partial \rho w u}{\partial x} + \frac{\partial \rho w v}{\partial y} + \frac{\partial \rho w w}{\partial z} = -\frac{\partial p}{\partial z} + \frac{\partial}{\partial z} \left[ 2\mu \frac{\partial w}{\partial z} - \frac{2}{3} \left( \frac{\partial u}{\partial x} + \frac{\partial v}{\partial y} + \frac{\partial w}{\partial z} \right) \right] \\ + \mu \frac{\partial}{\partial x} \left( \frac{\partial w}{\partial x} + \frac{\partial u}{\partial z} \right) + \mu \frac{\partial}{\partial y} \left( \frac{\partial w}{\partial y} + \frac{\partial v}{\partial z} \right) + \rho f_z \end{aligned} \quad (6)$$

$$\mu = \gamma \mu_w + (1 - \gamma) \mu_g \quad (7)$$

where  $p$  represents the pressure;  $\mu$  ( $\text{Ns}/\text{m}^2$ ) represents the molecular viscosity coefficient;  $\mu_w$  ( $\text{Ns}/\text{m}^2$ ) represents the molecular viscosity coefficient of water;  $\mu_g$  ( $\text{Ns}/\text{m}^2$ ) represents the molecular viscosity coefficient of air;  $f_x$ ,  $f_y$  and  $f_z$  are body force per unit mass including gravity and surface tension effects at the interface in the  $x$ ,  $y$ , and  $z$  directions, respectively.

### 2.3.3. $k$ - $\varepsilon$ Equations

$$\begin{aligned} \frac{\partial(\rho k)}{\partial t} + \frac{\partial(\rho k u)}{\partial x} + \frac{\partial(\rho k v)}{\partial y} + \frac{\partial(\rho k w)}{\partial z} = \\ \frac{\partial}{\partial x} \left[ \left( \mu + \frac{\mu_t}{\sigma_k} \right) \frac{\partial k}{\partial x} \right] + \frac{\partial}{\partial y} \left[ \left( \mu + \frac{\mu_t}{\sigma_k} \right) \frac{\partial k}{\partial y} \right] + \frac{\partial}{\partial z} \left[ \left( \mu + \frac{\mu_t}{\sigma_k} \right) \frac{\partial k}{\partial z} \right] + G_k - \rho \varepsilon \end{aligned} \quad (8)$$

$$\begin{aligned} \frac{\partial(\rho \varepsilon)}{\partial t} + \frac{\partial(\rho \varepsilon u)}{\partial x} + \frac{\partial(\rho \varepsilon v)}{\partial y} + \frac{\partial(\rho \varepsilon w)}{\partial z} = \\ \frac{\partial}{\partial x} \left[ \left( \mu + \frac{\mu_t}{\sigma_\varepsilon} \right) \frac{\partial \varepsilon}{\partial x} \right] + \frac{\partial}{\partial y} \left[ \left( \mu + \frac{\mu_t}{\sigma_\varepsilon} \right) \frac{\partial \varepsilon}{\partial y} \right] + \frac{\partial}{\partial z} \left[ \left( \mu + \frac{\mu_t}{\sigma_\varepsilon} \right) \frac{\partial \varepsilon}{\partial z} \right] + C_{\varepsilon 1} \frac{\varepsilon}{k} G_k - C_{\varepsilon 2} \rho \frac{\varepsilon^2}{k} \end{aligned} \quad (9)$$

$$G_k = \mu_t \left( \frac{\partial u_i}{\partial x_j} + \frac{\partial u_j}{\partial x_i} \frac{\partial u_i}{\partial x_j} \right) \quad (10)$$

$$\mu_t = \rho C_\mu \frac{k^2}{\varepsilon} \quad (11)$$

where  $k$  ( $\text{m}^2/\text{s}^2$ ) represents the turbulent energy;  $\varepsilon$  ( $\text{m}^2/\text{s}^3$ ) represents the rate of the energy dissipation;  $\mu_t$  ( $\text{Ns}/\text{m}^2$ ) represents the turbulent viscosity;  $\sigma_k$  represents the Prandtl number of the turbulent energy (here,  $\sigma_k = 1.0$ );  $\sigma_\varepsilon$  represents the Prandtl number of the rate of the energy dissipation (here,  $\sigma_\varepsilon = 1.39$ );  $C_{\varepsilon 1}$  and  $C_{\varepsilon 2}$  are empirical constants (here,  $C_{\varepsilon 1} = 1.44$  and  $C_{\varepsilon 2} = 1.92$ );  $G_k$  is the production term of the turbulent kinetic energy caused by the average velocity gradient;  $C_\mu$  is a constant (here,  $C_\mu = 0.09$ ).

#### 2.3.4. Transportation Equation of TDG

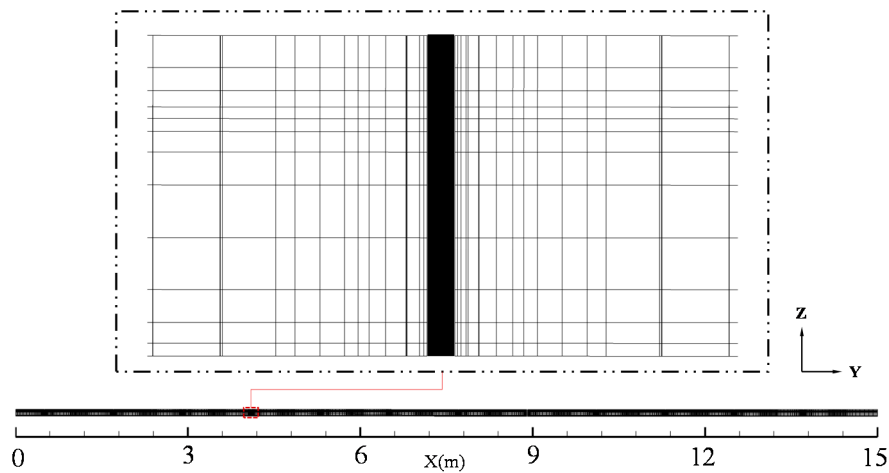
$$\frac{\partial(\rho G)}{\partial t} + \frac{\partial(\rho Gu)}{\partial x} + \frac{\partial(\rho Gv)}{\partial y} + \frac{\partial(\rho Gw)}{\partial z} = \frac{\partial}{\partial x} \left[ (\mu + D) \frac{\partial(\rho G)}{\partial x} \right] + \frac{\partial}{\partial y} \left[ (\mu + D) \frac{\partial(\rho G)}{\partial y} \right] + \frac{\partial}{\partial z} \left[ (\mu + D) \frac{\partial(\rho G)}{\partial z} \right] + \rho S_G \quad (12)$$

$$D = \frac{\mu}{\rho \sigma_t} \quad (13)$$

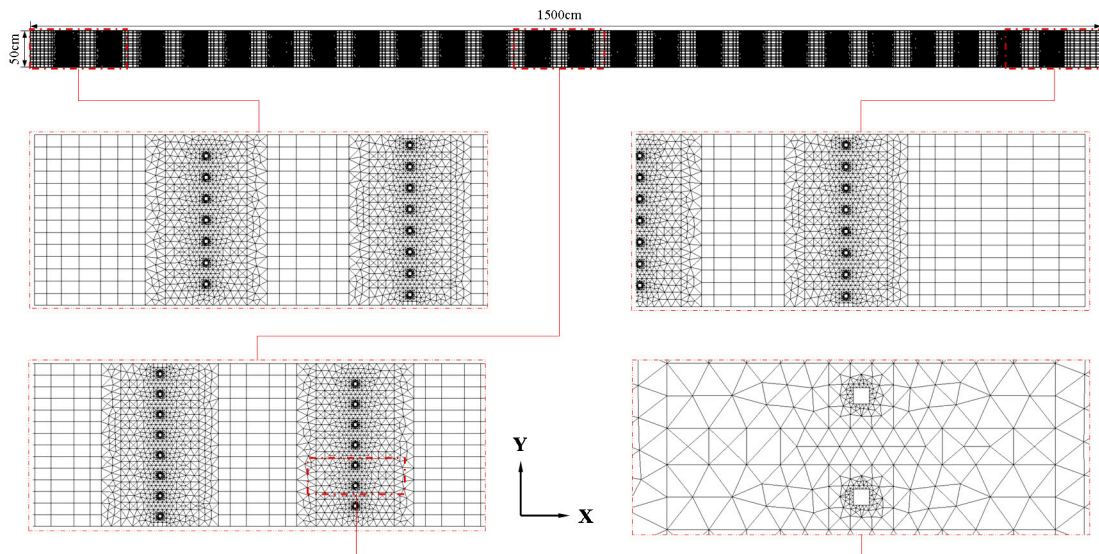
where  $G$  (%) is the percent saturation of TDG,  $\sigma_t$  is the Schmidt number (here,  $\sigma_t = 1.0$ ),  $S_G$  denotes the dissipation term of supersaturated TDG,  $k_{in}$  ( $\text{m}^{-3} \text{min}^{-1}$ ) represents the mass transfer coefficient, and  $G_{eq}$  (%) is the percent saturation of TDG under standard atmospheric pressure.  $S_G$ , representing source term, is set in Section 2.6.

#### 2.4. Compute Region and Meshes

The simulated area included the experimental water flume. Figure 3 demonstrates the mesh of the computational domain which contains a vertical grid mesh and a planar grid mesh. The gradient  $\sigma$  grid is used in the vertical direction, as shown in Figure 3a. The planar grid mesh is illustrated in Figure 3b. To ensure the accuracy of the flow field calculation around the vertical column, each side of each vertical column is divided into five grids. The region beyond the column is a mixed grid composed of rectangular and triangular grids.



(a) The vertical mesh



(b) The planar mesh

Figure 3. The mesh of calculative region with vegetation.

### 2.5. Boundary Conditions

#### 2.5.1. Boundary Conditions of Flow Field

The inflow was constant flow. The flow and water depth were programmed at the inflow section. The pressure above the water was barometric pressure, i.e., 101 kPa. A zero gradient was adopted as the outlet boundary condition. The solid walls of the flume and Plexiglas columns were analyzed using the standard wall function method, as follows:

$$u^* = \begin{cases} y^* & y^* < 11.225 \\ \frac{1}{\kappa} \ln(Ey^*) & y^* > 11.225 \end{cases} \quad (14)$$

$$u^* = \frac{U_P C_\mu^{1/4} k_P^{1/2}}{\tau_w / \rho} \quad (15)$$

$$y^* = \frac{\rho C_\mu^{1/4} k_P^{1/2} y_P}{\mu} \quad (16)$$

$$\tau_w = \rho C_\mu^{1/4} k_P^{1/2} u_P / u^* \quad (17)$$

where  $u^*$  and  $y^*$  are dimensionless parameters representing speed and distance, respectively;  $\kappa$  is the von Karman constant (here  $\kappa = 0.42$ );  $E$  is the roughness coefficient of the wall (here  $E = 9.81$ );  $U_P$  and  $k_P$  are the average velocity and turbulent kinetic energy at point P, respectively;  $y_P$  is the distance from point P to the wall and  $\tau_w$  is the shear stress of the wall.

### 2.5.2. Boundary Conditions of the TDG Concentration Field

The TDG saturation of the inflow section was taken as the inlet boundary condition, and a zero TDG gradient condition was programmed at the outlet. The solid walls of the flume and Plexiglas column were modeled using the adsorption flux formula of TDG proposed by Yuan [22], as follows:

$$F_a = \frac{1}{60} k_a a (G_{eq} - G) \quad (18)$$

where  $a$  is the superficial area of the wall in a unit volume of water ( $\text{m}^{-1}$ ) and  $k_a$  is the adsorption rate of the wall ( $\text{m}^{-2} \text{min}^{-1}$ ) (here  $k_a = 0.0046 \text{ m}^{-2} \text{min}^{-1}$ ).

## 2.6. Model Parameters

### 2.6.1. Parameterizing the TDG Source Term $S_G$

Neglecting the influence of bubbles, the supersaturated TDG in the river channel downstream of a dam can be dissipated in two ways: liquid-gas free surface transfer and dissipation within the water. The TDG mass exchange can be modeled as a linear combination of the two processes and expressed as:

$$S_G = S_{G1} + S_{G2} \quad (19)$$

(1) The liquid-gas free surface transfer

$$S_{G1} = K_{L,S} a_s C_s (G_{eq} - G) \quad (20)$$

where  $a_s$  is specific surface area;  $C_s$  is the effective air saturation concentration at the local water depth;  $G_{eq}$  is the equilibrium TDG saturation and  $K_{L,S}$  is the mass transfer coefficient, which can be calculated via the method by Geldert [48]:

$$K_{L,S} = 0.00243 u^{(-5/3)} k^{(4/3)} \quad (21)$$

where  $u$  is the surface flow velocity ( $\text{m s}^{-1}$ ) and  $k$  is the turbulent kinetic energy ( $\text{m}^2 \text{s}^{-2}$ ).

(2) Dissipation within the water

$$S_{G3} = k_{in} (G_{eq} - G) \quad (22)$$

where  $k_{in}$  is the inner dissipation coefficient ( $\text{s}^{-1}$ ).

### 2.6.2. The Formula of Inner Dissipation Coefficient

The prior studies focused on cases without vegetation and defined a comprehensive dissipation coefficient to describe the dissipation rate of TDG in a river or channel, which incorporated the total effects of inner dissipation within water, mass transfer in the free water surface and the solid river bed, among which the effect of inner dissipation was at the dominating place. As to the research on dissipation of supersaturated TDG in a channel with vegetation, the ratio of the effect caused by a solid wall is rising significantly. For the reason that the dissipation mechanism of TDG in water and on the wall is different, their influences on TDG dissipation need to be described and calculated separately in the model. Currently, there is no specific formula to calculate the inner dissipation coefficient. The value of the inner dissipation coefficient in water cannot be obtained under laboratory conditions. In this paper, taking the experimental TDG data (including the inlet TDG saturation and outflow TDG

saturation) of Huang (2017) [41] as the known conditions, the values of the inner dissipation coefficient in water were calibrated through the TDG transportation model mentioned before. The calibration results of the inner dissipation coefficient are shown in Table 2.

**Table 2.** Calibration results of inner dissipation coefficient.

Case No.	Flow Rate (L·s <sup>-1</sup> )	Vegetation Density	TDG Saturation Upstream (%)	TDG Saturation Downstream (%)	$k_{in}$ (s <sup>-1</sup> )
1	1.5	0	144.5	137.2	$4.5 \times 10^{-5}$
2	3.5	0	144.4	138.9	$5.5 \times 10^{-5}$
3	5.5	0	145.6	140.2	$6.0 \times 10^{-5}$
4	7.5	0	147.1	142.0	$6.5 \times 10^{-5}$
5	9.5	0	148.1	143.9	$7.8 \times 10^{-5}$
6	1.5	0.1	144.2	135.2	$4.3 \times 10^{-5}$
7	3.5	0.1	144.6	137.8	$5.2 \times 10^{-5}$
8	5.5	0.1	144.5	138.3	$5.8 \times 10^{-5}$
9	7.5	0.1	146.6	141.1	$6.3 \times 10^{-5}$
10	9.5	0.1	147.9	143.5	$7.5 \times 10^{-5}$
11	1.5	0.2	144.9	133.5	$4.0 \times 10^{-5}$
12	3.5	0.2	147.4	139.2	$5.0 \times 10^{-5}$
13	5.5	0.2	148.5	141.5	$5.5 \times 10^{-5}$
14	7.5	0.2	148.6	142.6	$6.0 \times 10^{-5}$
15	9.5	0.2	149.0	144.1	$7.2 \times 10^{-5}$
16	1.5	0.3	145.3	131.3	$3.7 \times 10^{-5}$
17	3.5	0.3	145.9	135.9	$4.7 \times 10^{-5}$
18	5.5	0.3	147.5	139.0	$5.2 \times 10^{-5}$
19	7.5	0.3	147.8	140.8	$5.8 \times 10^{-5}$
20	9.5	0.3	148.6	143.0	$7.0 \times 10^{-5}$
21	1.5	0.6	145.7	128.2	$3.0 \times 10^{-5}$
22	3.5	0.6	147.5	134.2	$4.1 \times 10^{-5}$
23	5.5	0.6	148.5	138.0	$4.5 \times 10^{-5}$
24	7.5	0.6	149.3	140.2	$5.0 \times 10^{-5}$
25	9.5	0.6	149.7	142.7	$6.3 \times 10^{-5}$

Generally, the dissipation of supersaturated TDG in water is impacted by hydraulic factors, such as flow velocity and water depth. For vegetation-affected flows, the dissipation of supersaturated TDG is also influenced by the vegetation density to some extent.

To study the expression of the inner dissipation coefficient in vegetation-affected flows, graphic analysis was conducted between the calibrated inner dissipation coefficient and the average velocity  $v$ , average depth  $H$ , and vegetation density  $d_V$ , as shown in Figure 4.

Figure 4a exhibits a good positive correlation between the inner dissipation coefficient and the average flow velocity, indicating that the greater the average flow velocity is, the faster the supersaturated TDG in water dissipates. Figure 4b shows that with the increase of average water depth, the inner dissipation coefficient decreases progressively when the vegetation density remains the same. Figure 4c shows the effect of vegetation density on the inner dissipation coefficient. We can clearly see that the higher the vegetation density is, the smaller the inner dissipation coefficient is for the same flow. The reason may be that the presence of vegetation causes a certain obstructive effect on the flow, resulting in a reduction in flow velocity and an increase in water depth, which leads to a reduction in the inner dissipation coefficient in water.

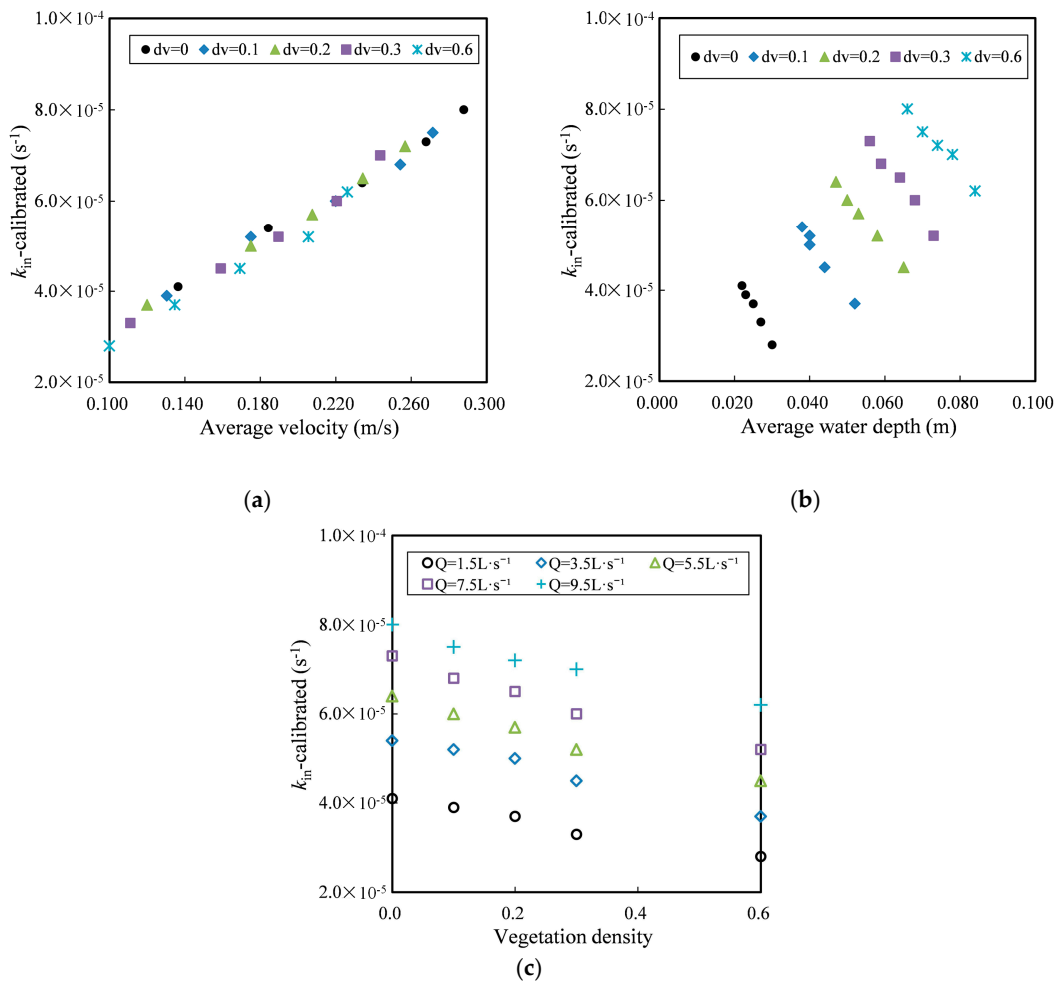


Figure 4. Relationships between the inner dissipation coefficient and various parameters.

In addition to the three parameters mentioned above, the average hydraulic radius  $R$  and Reynolds number  $Re$  were also selected as important parameters to fit formula of the inner dissipation coefficient in water. The Reynolds number can be used to represent the effect of turbulence on the inner dissipation coefficient, and the resulting expression can be written as follows:

$$k_{in} = \phi \left(\frac{v}{H}\right)^l \left(\frac{H}{R}\right)^m Re^n e^{\varphi dv} \tag{23}$$

where  $(H/R)^m$  represents the correction factor due to the influence of the wall and  $\phi$ ,  $l$ ,  $m$ ,  $n$ , and  $\varphi$  are dimensionless constants that can be fitted from the experimental results of Huang (2017) [41].

By employing the experimental data from 20 cases ( $Q = 1.5 \text{ L}\cdot\text{s}^{-1}$ ,  $Q = 3.5 \text{ L}\cdot\text{s}^{-1}$ ,  $Q = 5.5 \text{ L}\cdot\text{s}^{-1}$ ,  $Q = 7.5 \text{ L}\cdot\text{s}^{-1}$ ), the values of  $\phi$ ,  $l$ ,  $m$ ,  $n$ , and  $\varphi$  were found to be  $3.0 \times 10^{-6}$ , 0.29, 2.3, 0.24 and  $-0.7$ , respectively.

Substituting the values above into Equation (24), the formula for the inner dissipation coefficient of supersaturated can be expressed as follows:

$$k_{in} = 3.0 \times 10^{-6} \left(\frac{v}{H}\right)^{0.29} \left(\frac{H}{R}\right)^{2.3} Re^{0.34} e^{-0.7dv} \tag{24}$$

Equation (24) is used to calculate the inner dissipation coefficient of cases with a flow of  $9.5 \text{ L}\cdot\text{s}^{-1}$  (shown in Table 1), and the calculated results are listed in Table 3. The calculated results are very close to the calibrated results (shown in Figure 5), indicating that Equation (24) can be used to calculate the inner dissipation coefficient of supersaturated TDG in vegetation affected flows.

**Table 3.** Comparison of the inner dissipation coefficient of supersaturated total dissolved gas between calculated results and experimental data.

Case No.	Flow (L·s <sup>-1</sup> )	Vegetation Density	$k_{in}$ Calculated (s <sup>-1</sup> )	$k_{in}$ Calibrated (s <sup>-1</sup> )
5	9.5	0	$8.1 \times 10^{-5}$	$8.0 \times 10^{-5}$
10	9.5	0.1	$7.7 \times 10^{-5}$	$7.5 \times 10^{-5}$
15	9.5	0.2	$7.3 \times 10^{-5}$	$7.2 \times 10^{-5}$
20	9.5	0.3	$7.0 \times 10^{-5}$	$7.0 \times 10^{-5}$
25	9.5	0.6	$6.1 \times 10^{-5}$	$6.2 \times 10^{-5}$

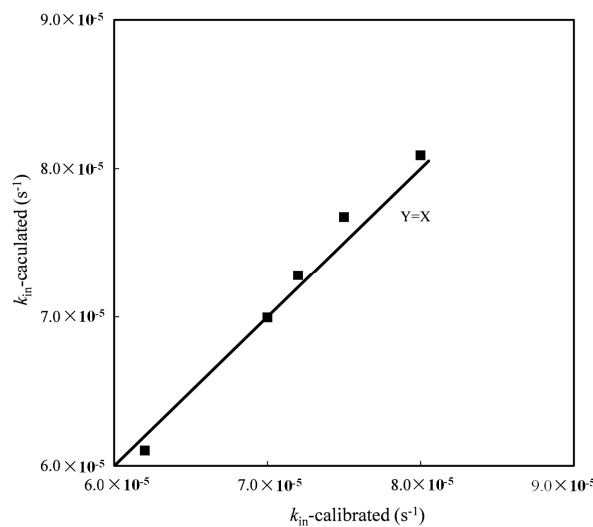


**Figure 5.** Comparisons between  $k_{in}$ -calculated and  $k_{in}$ -calibrated.

### 2.7. Verification of the Model

#### 2.7.1. Verification Case

The numerical model was verified using the experimental cases that did not participate in parameter calibration of the formula for the inner dissipation coefficient. Generally, the flow state is more complex when the flow and vegetation density are relatively high. Therefore, Case 25 ( $d_V = 0.6$ ,  $Q = 9.5 \text{ L}\cdot\text{s}^{-1}$ ) and Case 15 ( $d_V = 0.2$ ,  $Q = 9.5 \text{ L}\cdot\text{s}^{-1}$ ) are selected as the verification cases for the numerical simulation. Case 15 and Case 25, which have the same lateral arrangement of Plexiglas columns but different longitudinal arrangements, are also selected as a verification of the influence of wake flow around the columns.

The boundary conditions of verification cases are verified in Table 4.

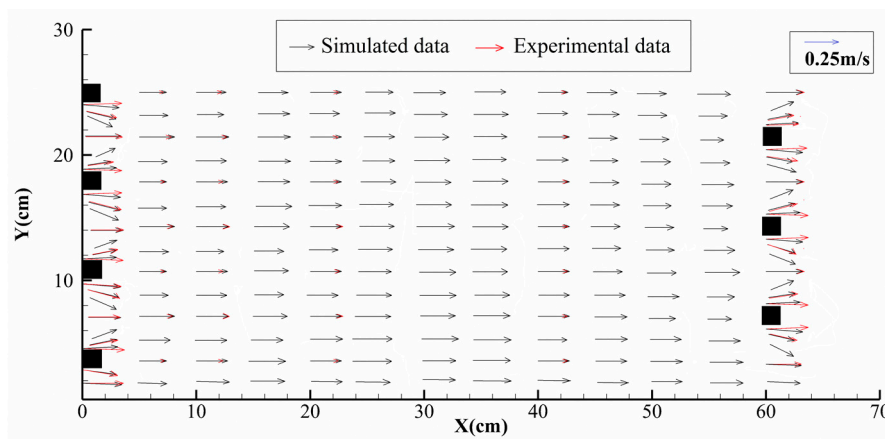
**Table 4.** The boundary conditions of the verification cases.

Case No.	Flow (m <sup>3</sup> ·s <sup>-1</sup> )	The Water Depth of Inlet Section (10 <sup>-2</sup> m)	The TDG Saturation of Inlet Section (%)
15	0.0095	7.4	149.0
25	0.0095	8.4	149.7

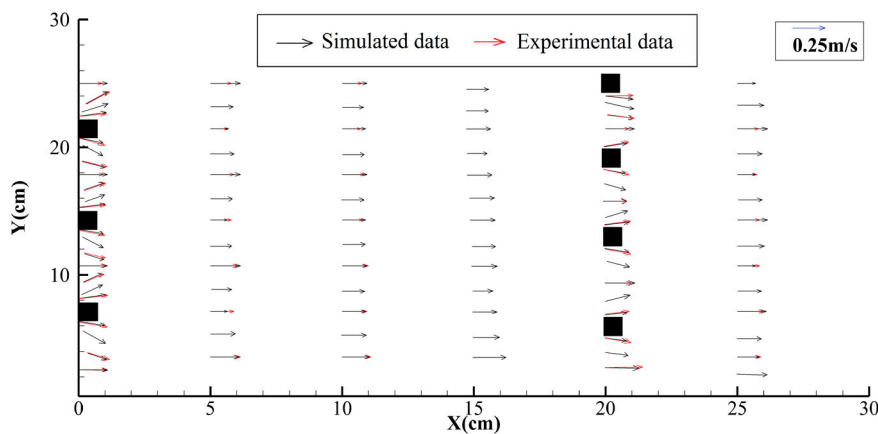
#### 2.7.2. Verification Results of the Flow Field

For Case 15, we selected the flow field where the sixth and seventh rows of Plexiglas columns were located ( $X = 3.6\text{--}4.3 \text{ m}$ ), and for Case 25, we selected the flow field where the seventh and eighth rows of Plexiglas columns were located ( $X = 1.4\text{--}1.65 \text{ m}$ ). The Plexiglas columns in the flume were arranged symmetrically in the lateral direction, so the flow field was also symmetrical in the lateral direction. For this reason, the numerical simulation results are compared with the experimental results only in the area of  $Y = 0 \text{ cm}$  to  $Y = 25 \text{ cm}$ .

Figure 6 compares the simulated results and the measured results for the surface velocity vector. We can see that the direction of flow velocity around the column is deflected due to the obstruction of the vertical columns, forming an angle with the direction of X axis; while in the area downstream of the column, the direction of flow velocity is the same as that of X axis. Figure 7 shows the distribution of vertical average velocity on the lateral section behind the vertical column. It can be seen that the area blocked by the vertical column has a smaller vertical average velocity. However, the vertical average velocity in the area not blocked by the vertical column is larger. The measured value of vertical average velocity is very close to the simulated value. Figure 8 demonstrates the distribution of vertical average velocity on the lateral section 5 cm downstream of the vertical column. It can be seen that the distribution trend of measured value is very similar to simulated value, showing a serrated distribution. Figure 9 exhibits the distribution of vertical average velocity on the longitudinal sections between the front row and back row of vertical columns, including the post-column longitudinal sections (Section 15-4 and Section 25-4) and the pre-column longitudinal sections (Section 15-5 and Section 25-5). It can be seen from Figure 9 that the simulated velocity distribution is basically consistent with the measured velocity distribution between the front row and back row of vertical columns. On the post-column longitudinal section, the distribution of vertical average velocity presents a trend that increases abruptly downstream along the flume and then becomes flat. While on the pre-column longitudinal section, the distribution of vertical average velocity tends to be flat first and then drops sharply when close to the vertical column.



(a) Section 15-1 (Case 15)



(b) Section 25-1 (Case 25)

Figure 6. Distribution of the simulated results and experimental results of the surface velocity vector.

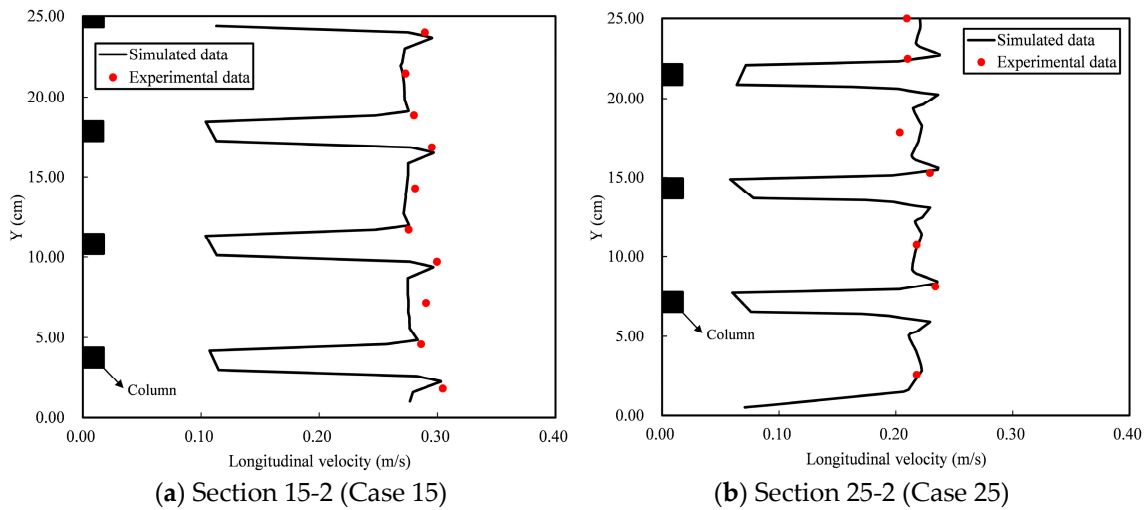


**Figure 7.** Distribution of the simulated vertical average velocity and experimental average velocity of the section behind the vertical columns. Section 15-2 is the lateral section behind the sixth row of vertical columns in Case 15; Section 25-2 is the lateral section behind the seventh row of vertical columns in Case 25.

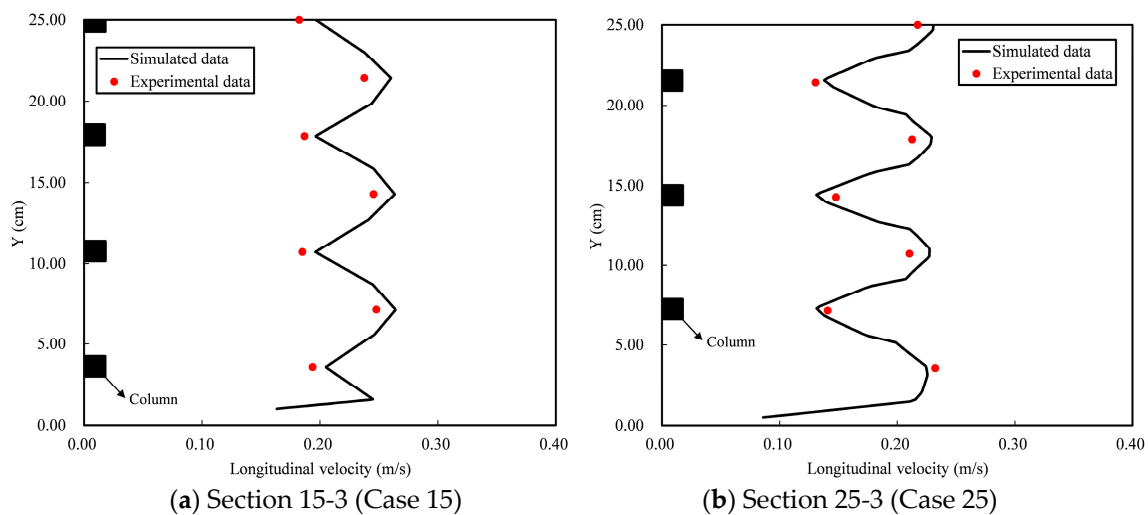


**Figure 8.** Distribution of the simulated vertical average velocity and experimental vertical average velocity of the lateral section downstream of the vertical columns. Section 15-3 is the lateral section 5 cm downstream of the sixth row of vertical columns in Case 15. Section 25-3 is the lateral section 5 cm downstream of the seventh row of vertical columns in Case 25.

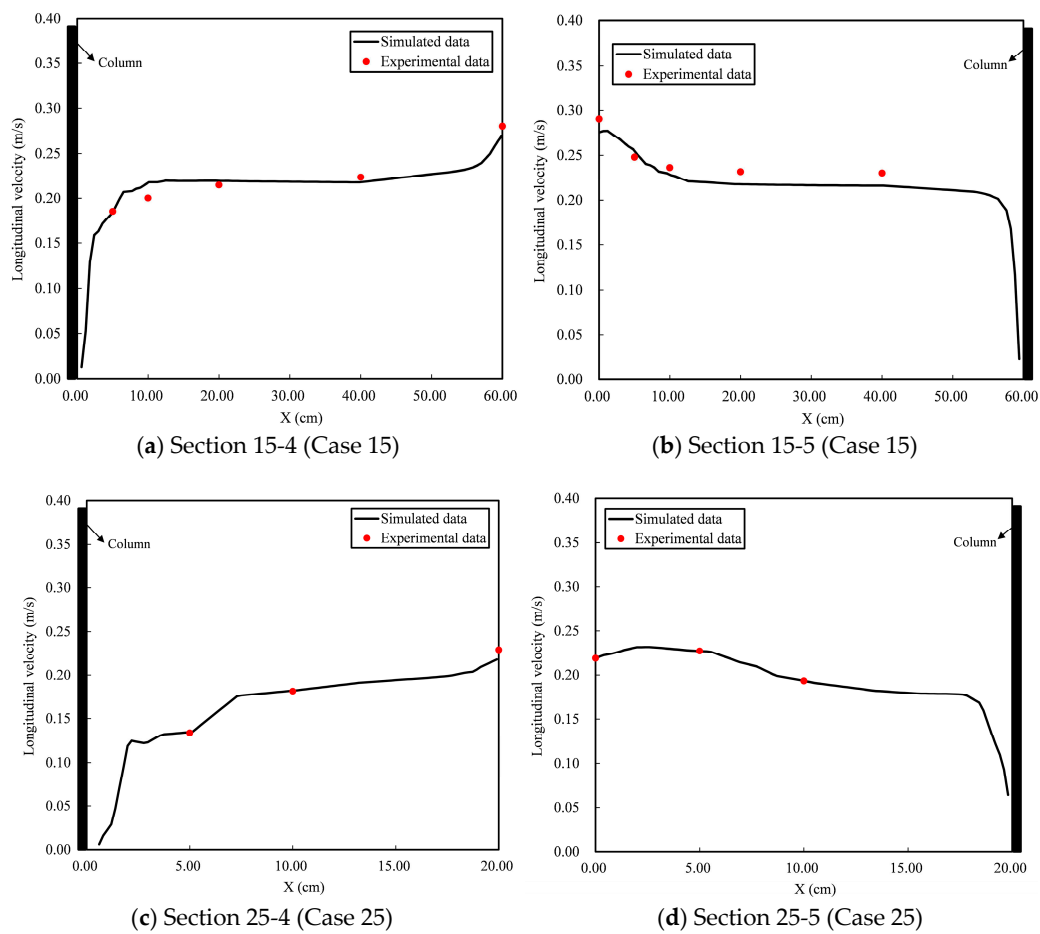


**Figure 9.** Distribution of the simulated vertical average velocity and the experimental vertical average velocity of the longitudinal section between the front row and back row of vertical columns. (a) Section 15-4 is the longitudinal section behind the second vertical column of sixth row ( $Y = 10.7$  cm) in Case 15; (b) Section 15-5 is the longitudinal section before the second vertical column of the seventh row ( $Y = 14.3$  cm) in Case 15; (c) Section 25-4 is the longitudinal section behind the second vertical column of seventh row ( $Y = 7.1$  cm) in Case 25; (d) Section 25-5 is the longitudinal section before the second vertical column of seventh row ( $Y = 10.7$  cm) in Case 25.

Error analysis of each section was performed. Mean error, relative average deviation (RSD), standard deviation (STD) and root-mean-square error (RMSE) were taken as analysis indexes to analyze the error in each section. The error analysis results are shown in Table 5. The error between the simulation results and the measured results is within  $0.019 \text{ m s}^{-1}$ , demonstrating that the above mentioned model can perfectly reflect the flow field distribution of the vegetation-affected flow.

**Table 5.** Error analysis results. RSD: relative average deviation; STD: standard deviation; RMSE: root-mean-square error.

Section No.	Mean Error (m/s)	RSD (%)	STD	RMSE (m/s)
Section 15-1	0.018	7.2	0.02	0.023
Section 15-2	0.019	6.5	0.02	0.009
Section 15-3	0.015	6.8	0.02	0.004
Section 15-4	0.008	3.3	0.01	0.006
Section 15-5	0.013	6.4	0.02	0.008
Section 25-1	0.017	8.6	0.02	0.019
Section 25-2	0.010	4.7	0.01	0.007
Section 25-3	0.012	6.8	0.01	0.004
Section 25-4	0.011	5.5	0.01	0.008
Section 25-5	0.011	6.4	0.01	0.002

### 2.7.3. Verification Results of the TDG Concentration Field

The TDG saturation of the outflow section was used to verify the TDG concentration field. The comparison between the simulation results and the measured values is shown in Figure 10. The calculated values of the outflow section in Case 15 and Case 25 are 144.4% and 142.3%, respectively, which are very close to the measured values of 144.1% and 142.7%, with errors both less than 0.3%.

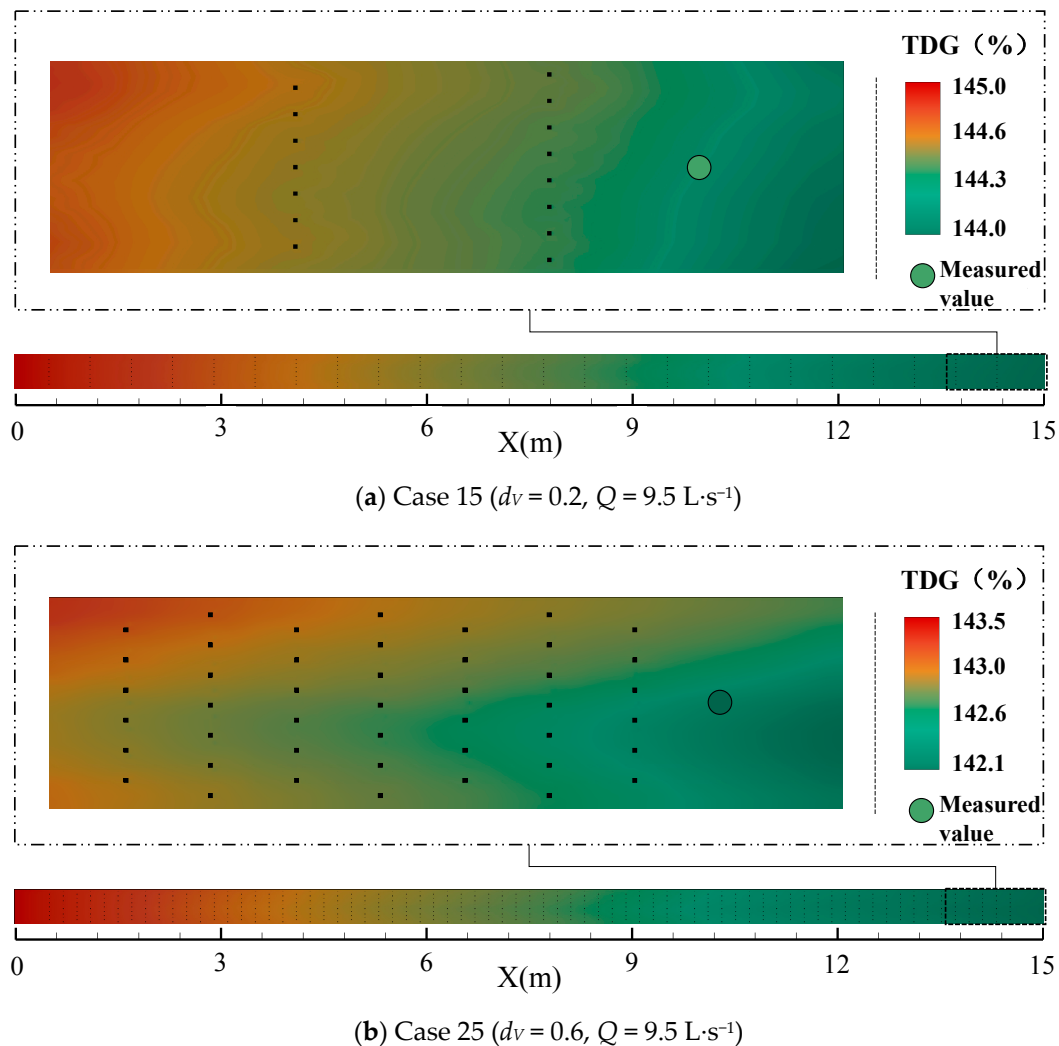


Figure 10. Comparison between simulation results and experimental data of TDG saturation.

## 3. Results and Discussions

### 3.1. The Distribution of Supersaturated TDG around a Column

The distribution of supersaturated TDG around a single column has similar features in various cases with different flow rates and vegetation densities, so only the distribution of supersaturated TDG around the single column in Case 25 ( $d_V = 0.6$ ,  $Q = 9.5 \text{ L}\cdot\text{s}^{-1}$ ) is shown in Figure 11 (the distance from the bottom of the flume is 0.09 m). The area downstream of the columns exhibited an obviously low saturation. The reason may be that the existence of columns blocks the flow, resulting in an area of low-speed wakes and vortices behind the columns. In this region, the decreased flow rate results in a longer retention time, allowing the supersaturated TDG to more fully dissipate.

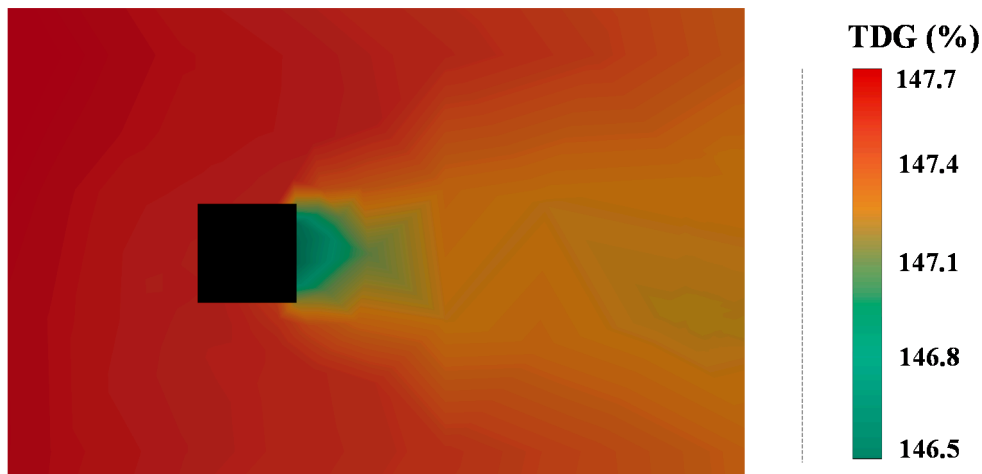


Figure 11. The distribution of supersaturated TDG around a single column ( $Z = 0.09$  m).

### 3.2. Vertical Distribution of Supersaturated TDG

In different vegetation cases, the TDG saturation presents similar distribution characteristics in the vertical direction. Therefore, the TDG distribution in the vertical direction is shown for Case 25 ( $d_V = 0.6$ ,  $Q = 9.5 \text{ L}\cdot\text{s}^{-1}$ ) in Figure 12. Figure 12 shows that the TDG saturation in the surface water is slightly lower than that in the subsurface water. The TDG saturation in the subsurface water decreases as the water depth increases. This feature is the result of the uneven distribution of vertical velocity and mass transfer in the free water surface. In vegetation-affected flows, the vertical distribution of flow velocity exhibits a pattern in which the deeper the water depth is, the lower the flow velocity is. Affected by this distribution, the upper water with a higher TDG saturation reaches the downstream section before the lower water. Furthermore, the lower flow velocity causes longer retention time of the lower water, and the supersaturated TDG in this part of the water is allowed to more fully dissipate.

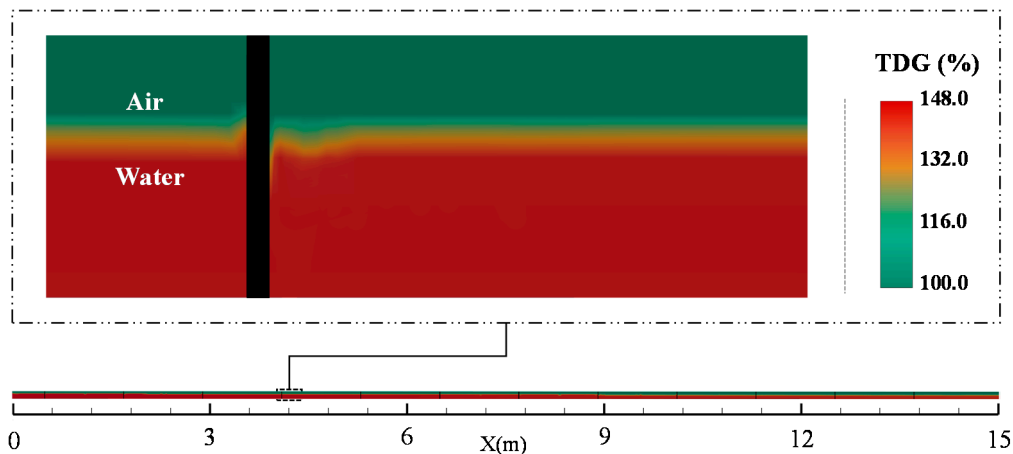


Figure 12. Vertical distribution of supersaturated TDG (Case 25).

### 3.3. Planar Distribution of Supersaturated TDG

Figure 13 shows the scattergram of supersaturated TDG on a horizontal plane. The distribution of TDG presents an obvious discipline under the large flow condition, so we have selected the cases with the flow of  $9.5 \text{ L}\cdot\text{s}^{-1}$  for graphical analysis. In order to compare the distribution discipline of supersaturated TDG under the condition without vegetation and with vegetation, we chose the case without vegetation (Case 5, Figure 13a) and the case with maximum vegetation density (Case 25, Figure 13b) for comparative analysis. As can be seen from Figure 13a,b, the distributions

of supersaturated TDG are quite different between cases without vegetation and with vegetation. For Case 5 without vegetation, the equal TDG saturation lines are concave backwards curves, while for Case 25 with maximum vegetation, the equal TDG saturation lines are convex forward curves. In addition, for comparing the distribution discipline of TDG saturation under different vegetation densities, we conducted a comparative analysis of case with low vegetation density (Case 15, Figure 13c) and Case 25. It can be seen that the curvature of the equal TDG saturation lines at the inflection point is larger when the vegetation density is larger.

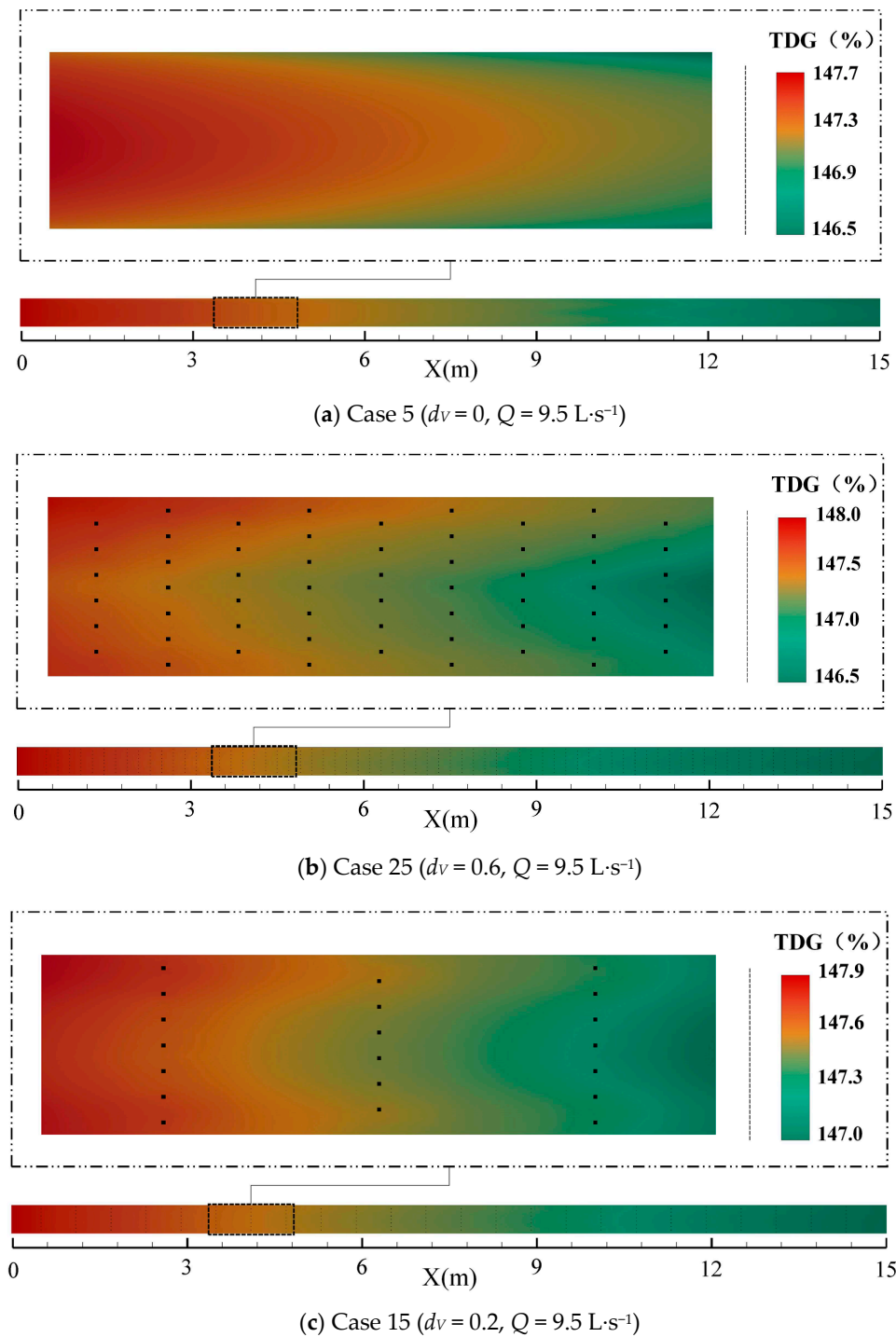
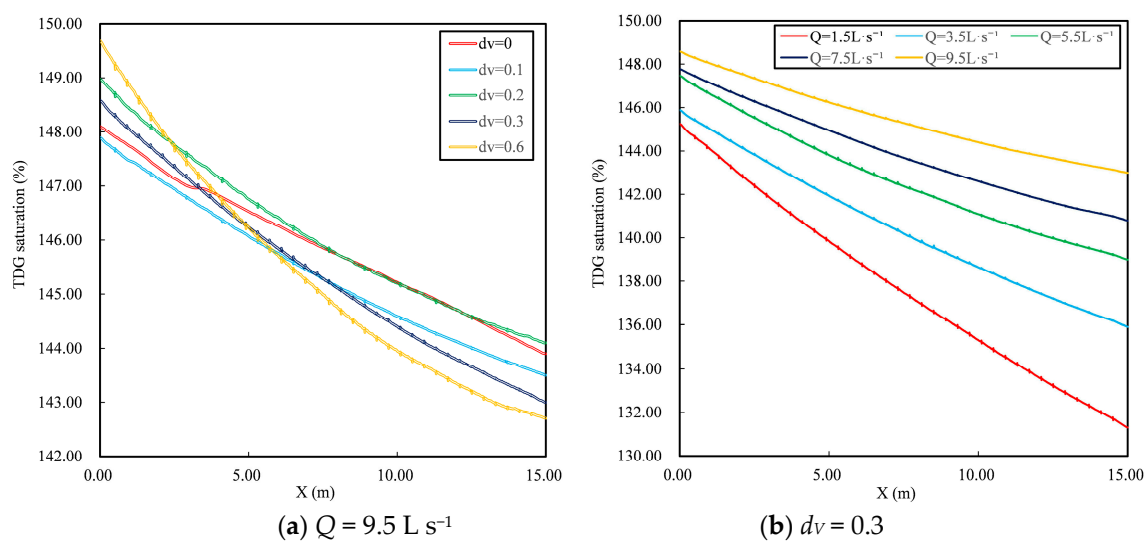


Figure 13. The scattergram of supersaturated TDG on a horizontal plane.

### 3.3.1. The Longitudinal Distribution of Supersaturated TDG

The TDG saturation values along the central axis ( $Y = 0.25$  m) of the water surface are used to analyze the longitudinal distribution of oversaturated TDG. We considered the effect of vegetation density and flow, as shown in Figure 14a,b, respectively.

Figure 14a is a longitudinal scatter gram of supersaturated TDG in cases with different vegetation densities and the same flow of  $9.5 \text{ L}\cdot\text{s}^{-1}$  and indicates that the existence of vegetation can significantly promote the dissipation of supersaturated TDG. With the same flow, the higher the density of vegetation is, the greater the obstruction of vegetation to water is, so that the retention time of supersaturated TDG in water increases and the supersaturated TDG is fully dissipated along the path. Due to the influence of the vertical column, the TDG saturation near the vertical column presents a zigzag distribution feature. In addition, because the initial saturation of the inlet section in cases with higher vegetation density is larger, the curve of TDG saturation in cases with higher vegetation intersects the curve of TDG saturation in cases with lower vegetation along the longitudinal direction. Figure 14b shows the longitudinal scattergram of supersaturated TDG in cases with different flows and the same vegetation density of 0.3. As seen from the Figure 14b, lower flow values are associated with greater dissipation of the supersaturated TDG throughout the whole process. The reason may be that the average water retention time is extended by the decrease in the flow, causing the supersaturated TDG in the water more fully dissipate. At the same time, when the flow rate is smaller, the retention effect of the column is better, and the serrated distribution characteristics of the supersaturated TDG are more obvious.



**Figure 14.** The longitudinal scattergram of supersaturated TDG.

### 3.3.2. The Lateral Distribution of Supersaturated TDG

The TDG saturation values along the horizontal axis ( $X = 7.65$  m) of the water surface are used to analyze the lateral distribution of oversaturated TDG. We also considered the effect of vegetation density and flow, as shown in Figure 15a,b, respectively.

Figure 15a shows a lateral scatter gram of supersaturated TDG in cases with different vegetation densities and the same flow of  $9.5 \text{ L}\cdot\text{s}^{-1}$ . In cases without vegetation, the middle TDG saturation is slightly higher than that of both sides. In cases with vegetation, the lateral distribution of TDG saturation is the opposite, characterized by low saturation in the middle and high saturation on both sides; the higher the vegetation density is, the more obvious this distribution characteristic is. The reason may be that vegetation acts as a barrier to water flow, causing the lateral flow velocity outside the flume's wall boundary layer to present a phenomenon of low in the middle and high on both sides. As a result, when upstream water with higher TDG saturation is transported downstream, the water along the edge flows downstream before the central water, making the TDG saturation on

both sides higher than that in the center. Figure 15b presents a lateral scattergram of supersaturated TDG in cases with different flows and the same vegetation density of 0.3. When the vegetation density is constant while the flow varies, the distribution characteristics of supersaturated TDG present the same trend, namely the TDG saturation in the middle is slightly lower than that on both sides. It seems that the effect of flow on the lateral distribution of supersaturated TDG is not as great as that of vegetation.

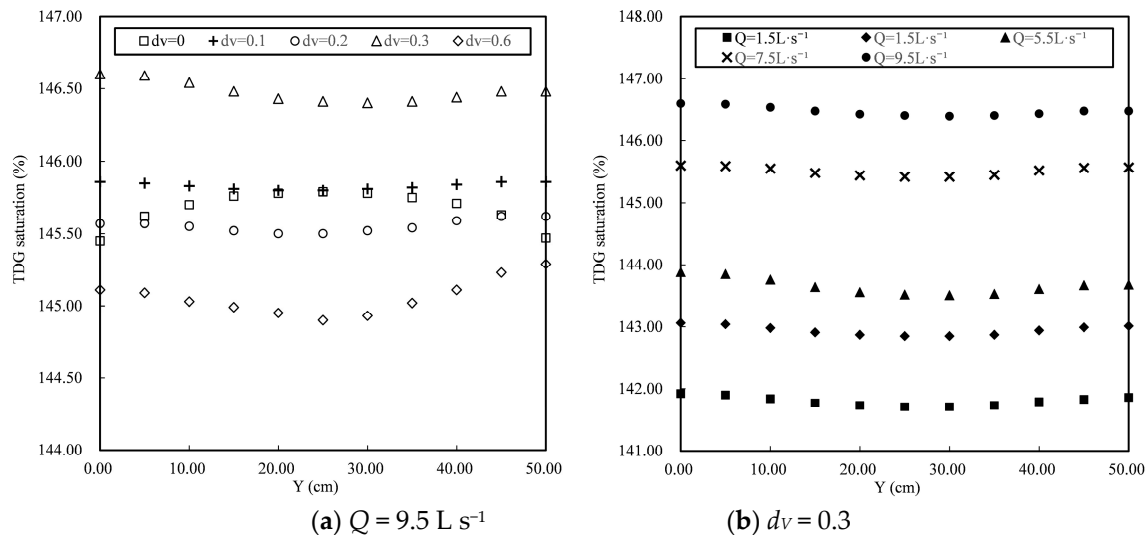


Figure 15. The lateral scattergram of supersaturated TDG.

#### 4. Conclusions and Prospect

Coastal floodplains are an important location for fish breeding and fertilization. The existence of vegetation in the floodplain makes the water flow structure in the beach area complex. When the flow is discharged from high dams, the supersaturated TDG can be caused and do harm to fish, so the dissipation characteristics of supersaturated TDG under the water-blocking effect of vegetation on the floodplain need to be clarified. In this paper, the effects of vegetation on the dissipation of supersaturated TDG were studied. The research results are of general reference value for improving the prediction accuracy of supersaturated TDG transportation and dissipation downstream of high dams, for identifying measures to mitigate the adverse effects of supersaturated TDG, and for protecting aquatic life in hydropower-developed rivers. The conclusions of this paper are as follows:

- (1) A three-dimensional two-phase flow dynamics model was established to study the complex characteristics of three-dimensional flow under the effects of vegetation, and the model was verified by measurements of flow velocity in vegetation-affected flows in the experiments. The verification results indicated that the numerical simulation results of each section were basically consistent with the measured flow velocity distribution, and the calculation error of flow velocity was within  $0.019 \text{ m}\cdot\text{s}^{-1}$ .
- (2) Dividing the dissipation process of supersaturated TDG in vegetation-affected flows into the liquid-gas free surface transfer and the inner dissipation, a three-dimensional supersaturated TDG transportation and dissipation model considering the influence of vegetation was established. In this model, the inner dissipation coefficient was introduced to characterize the inner dissipation of supersaturated TDG. A formula based on the average velocity, the average hydrodynamic radius, Reynolds number and vegetation density was developed to predict the inner dissipation coefficient of supersaturated TDG. The prediction model was verified with two individual cases, and this verification demonstrated that the simulation results of the dissipation process of supersaturated TDG in the flume were very close to the measured values. The transportation and dissipation model of supersaturated TDG established in this paper can be

used to predict the transportation and dissipation process of supersaturated TDG dissipation in vegetation-affected flows.

- (3) The simulation results show that the water-blocking effect caused by a column formed an obvious area of low TDG saturation behind the column. In the vertical direction, the TDG saturation in the surface water was slightly lower than that in the subsurface water, and TDG saturation in the subsurface water decreased as the water depth increased. At the same time, affected by the water-blocking effect of the vegetation group, TDG saturation presented a distribution characterized by high values in the middle and low values on both sides in the lateral direction. In the longitudinal direction, the TDG saturation decreased gradually with downstream extent but showed serrated distribution characteristics in the region behind the column.
- (4) Because the existing measurement and numerical simulation methods have difficulty reflecting the influence of real vegetation on the flow field and the supersaturated TDG transportation and dissipation process, a Plexiglas vertical column with a square cross section was selected to simulate rigid hydrophilic plants. The effects of vegetation's flexible characteristics and the presence of leaves on the transportation and dissipation processes of supersaturated TDG in flowing water remain to be studied. Limited by laboratory conditions, only small-scale mechanism experiments have been carried out. The parameters used in the three-dimensional TDG transportation and dissipation model were also calibrated by the experimental results. The applicability of this model for simulating the transportation and dissipation process of supersaturated TDG under vegetation-affected flows in large-scale flows remains to be further studied.

**Author Contributions:** Y.Q.-Y. contributed to the establishment of model, significantly to analysis and manuscript preparation. Y.H.-H. contributed to the collection of experimental data. J.J.-F. contributed to the conception of the study. R.L. contributed to the analysis and interpretation of the results. R.D.-A. contributed to the revise of this article. J.P.-H. contributed to the final editing.

**Funding:** This work was supported by National Key R & D Program of China (Grant No. 2016YFC0401707) and the National Natural Science Foundation of China (Grant No. 51879173).

**Acknowledgments:** We acknowledge the support of National Key R & D Program and National Natural Science Foundation.

**Conflicts of Interest:** The authors declare no conflict of interest.

## References

1. Wydoski, R.S.; Wick, E.J. Flooding and aquatic ecosystems. In *Inland Flood Hazards: Human, Riparian, and Aquatic Communities*; Wohl, E.E., Ed.; Cambridge University Press: New York, NY, USA, 2011; pp. 238–268.
2. Reolid, M.; Rodríguez-Tovar, F.J.; Nagy, J. Ecological replacement of Valanginian agglutinated foraminifera during a maximum flooding event in the Boreal realm (Spitsbergen). *Cretac. Res.* **2012**, *33*, 196–204. [[CrossRef](#)]
3. Heydel, F.; Engels, J.G.; Feigs, J.T.; Vásquez, E.; Rudolph, B.; Rohwer, J.; Jensen, K. Adaptation to tidal flooding and rapid genetic divergence between a narrow endemic grass species and its widespread congener lead to an early stage of ecological speciation. *Perspect. Plant Ecol.* **2017**, *27*, 57–67. [[CrossRef](#)]
4. Bendix, J.; Cowell, C.M. Fire, floods and woody debris: Interactions between biotic and geomorphic processes. *Geomorphology* **2010**, *116*, 297–304. [[CrossRef](#)]
5. Chaleeraktragoon, C.; Chinsomboon, Y. Dynamic rule curves for flood control of a multipurpose dam. *J. Hydro-Environ. Res.* **2015**, *9*, 133–144. [[CrossRef](#)]
6. Talukdar, S.; Pal, S. Impact of dam on inundation regime of flood plain wetland of punarbhaha river basin of barind tract of Indo-Bangladesh. *Int. Soil Water Conserv. Res.* **2017**, *5*, 109–121. [[CrossRef](#)]
7. Tao, J.P.; Yang, Z.; Cai, Y.P.; Wang, X.; Chang, J.B. Spatiotemporal response of pelagic fish aggregations in their spawning grounds of middle Yangtze to the flood process optimized by the Three Gorges Reservoir operation. *Ecol. Eng.* **2017**, *103*, 86–94. [[CrossRef](#)]
8. Quirino, B.A.; Carniatio, N.; Guglielmetti, R.; Fugli, R. Changes in diet and niche breadth of a small fish species in response to the flood pulse in a Neotropical floodplain lake. *Limnologia* **2017**, *62*, 126–131. [[CrossRef](#)]

9. Lemke, M.J.; Hagy, H.M.; Dungey, K.; Casper, A.F.; Lemke, A.M.; VanMiddlesworth, T.D.; Kent, A. Echoes of a flood pulse: Short-term effects of record flooding of the Illinois River on floodplain lakes under ecological restoration. *Hydrobiologia* **2017**, *804*, 151–175. [[CrossRef](#)]
10. Bolland, J.D.; Nunn, A.D.; Lucas, M.C.; Cowx, I.G. The habitat use of young-of-the-year fishes during and after floods of varying timing and magnitude in a constrained lowland river. *Ecol. Eng.* **2015**, *75*, 434–440. [[CrossRef](#)]
11. Li, R.; Li, J.; Li, K.F.; Deng, Y.; Feng, J.J. Prediction for supersaturated total dissolved gas in high-dam hydropower projects. *Sci. China Ser. E* **2009**, *52*, 3661–3667. [[CrossRef](#)]
12. Feng, J.J.; Li, R.; Ma, Q.; Wang, L.L. Experimental and field study on dissipation coefficient of supersaturated total dissolved gas. *J. Cent. South Univ.* **2014**, *21*, 1995–2003. [[CrossRef](#)]
13. Kamal, R.; Zhu, D.Z.; McArthur, M.; Leake, A. Field study on the dissipation of supersaturated total dissolved gases in a cascade reservoir system. In Proceedings of the World Environmental and Water Resources Congress 2016, West Palm Beach, FL, USA, 22–26 May 2016; pp. 452–460.
14. Weitkamp, D.E.; Sullivan, R.D.; Swant, D.; DosSantos, J. Gas Bubble Disease in Resident Fish of the Lower Clark Fork River. *Trans. Am. Fish. Soc.* **2003**, *132*, 865–876. [[CrossRef](#)]
15. Wang, Y.M.; Liang, R.F.; Tuo, Y.C.; Li, K.F.; Hodegs, B.R. Tolerance and Avoidance Behavior towards Gas Supersaturation in Rock Carp *Procypris rabaudi* with a History of Previous Exposure. *N. Am. J. Aquac.* **2015**, *77*, 478–484. [[CrossRef](#)]
16. Li, R.; Hodegs, B.R.; Feng, J.J.; Yong, X.D. Comparison of supersaturated total dissolved gas dissipation with dissolved oxygen dissipation and reaeration. *J. Environ. Eng.* **2013**, *139*, 385–390. [[CrossRef](#)]
17. Ou, Y.M.; Li, R.; Hodges, B.R.; Feng, J.J.; Pu, C.X. Impact of temperature on the dissipation process of supersaturated total dissolved gas in flowing water. *Fresenius Environ. Bull.* **2016**, *25*, 1927–1934.
18. Huang, J.P.; Li, R.; Feng, J.J.; Xu, W.L.; Wang, L.L. Relationship investigation between the dissipation process of supersaturated total dissolved gas and wind effect. *Ecol. Eng.* **2016**, *95*, 430–437. [[CrossRef](#)]
19. Ou, Y.M.; Li, R.; Tuo, Y.C.; Niu, J.L.; Feng, J.J.; Pu, C.X. The promotion effect of aeration on the dissipation of supersaturated total dissolved gas. *Ecol. Eng.* **2016**, *95*, 245–251. [[CrossRef](#)]
20. Shen, X.; Li, R.; Huang, J.P.; Feng, J.J.; Hodges, B.R.; Li, K.F.; Xu, W.L. Shelter construction for fish at the confluence of a river to avoid the effects of total dissolved gas supersaturation. *Ecol. Eng.* **2016**, *97*, 642–648. [[CrossRef](#)]
21. Witt, A.; Stewart, K.; Hadjerioua, B. Predicting Total Dissolved Gas Travel Time in Hydropower Reservoirs. *J. Environ. Eng.* **2017**, *143*, 06017011. [[CrossRef](#)]
22. Yuan, Y.Q.; Feng, J.J.; Li, R.; Huang, Y.H.; Huang, J.P.; Wang, Z.H. Modelling the promotion effect of vegetation on the dissipation of supersaturated total dissolved gas. *Ecol. Model.* **2018**, *386*, 89–97. [[CrossRef](#)]
23. Pickett, J.; Rueda, H.; Herold, M. *Total Maximum Daily Load for Total Dissolved Gas in the Mid-Columbia River and Lake Roosevelt*; U.S. Environmental Protection Agency and Washington State Department of Ecology: Washington, DC, USA, 2004; pp. 1–79.
24. Perkins, W.A.; Richmond, M.C. *MASS2, Modular Aquatic Simulation System in Two Dimensions: Theory and Numerical Methods*; Pacific Northwest National Laboratory Report; Pacific Northwest National Laboratory: Washington, DC, USA, 2004; pp. 1–73.
25. Johnson, E.L.; Clabough, T.S.; Peery, C.A.; Bennett, D.H.; Bjornn, T.C.; Caudill, C.C.; Richmond, M.C. Estimating adult Chinook salmon exposure to dissolved gas supersaturation downstream of hydroelectric dams using telemetry and hydrodynamic models. *River Res. Appl.* **2010**, *23*, 963–978. [[CrossRef](#)]
26. Ma, Q.; Li, R.; Zhang, Q.; Hodges, B.R.; Feng, J.J.; Yang, H.X. Two-Phase Flow Simulation of Supersaturated Total Dissolved Gas in the Plunge Pool of a High Dam. *Environ. Prog. Sustain.* **2016**, *35*, 1139–1148. [[CrossRef](#)]
27. Witt, A.; Magee, T.; Stewart, K.; Hadjerioua, B. Development and implementation of an optimization model for hydropower and total dissolved gas in the Mid-Columbia River System. *J. Water Res. Plan.* **2017**, *143*, 04017063. [[CrossRef](#)]
28. Feng, J.J.; Li, R.; Liang, R.F.; Shen, X. Eco-environmentally friendly operational regulation: An effective strategy to diminish the TDG supersaturation of reservoirs. *Hydrol. Earth Syst. Sci.* **2014**, *10*, 14355–14390. [[CrossRef](#)]
29. Aberle, J.; Järvelä, J. *Hydrodynamics of Vegetated Channels, In Rivers-Physical, Fluvial and Environmental Processes*; Springer International Publishing Switzerland: Bern, Switzerland, 2015; pp. 255–277.

30. Nepf, H.M. Flow and Transport in Regions with Aquatic Vegetation. *Annu. Rev. Fluid Mech.* **2012**, *44*, 123–142. [[CrossRef](#)]
31. Afzalimehr, H.; Najafabadi, E.F.; Gallichand, J. Effects of accelerating and decelerating flows in a channel with vegetated banks and gravel bed. *Int. J. Sediment Res.* **2012**, *27*, 188–200. [[CrossRef](#)]
32. Serio, F.D.; Meftah, M.B.; Mossa, M.; Termini, D. Experimental investigation on dispersion mechanisms in rigid and flexible vegetated beds. *Adv. Water Resour.* **2017**, *120*, 98–113. [[CrossRef](#)]
33. Hamidifar, H.; Omid, M.H.; Keshavarzi, A. Kinetic energy and momentum correction coefficients in straight compound channels with vegetated floodplain. *J. Hydrol.* **2016**, *537*, 10–17. [[CrossRef](#)]
34. Dijk, W.M.V.; Teske, R.; Lageweg, W.I.V.D.; Kleinhans, M.G. Effects of vegetation distribution on experimental river channel dynamics. *Water Resour. Res.* **2013**, *49*, 7558–7574. [[CrossRef](#)]
35. Yang, J.Q.; Kerger, F.; Nepf, H.M. Estimation of the bed shear stress in vegetated and bare channels with smooth beds. *Water Resour. Res.* **2015**, *51*, 3647–3663. [[CrossRef](#)]
36. Richet, J.B.; Ouvry, J.F.; Saunier, M. The role of vegetative barriers such as fascines and dense shrub hedges in catchment management to reduce runoff and erosion effects: Experimental evidence of efficiency, and conditions of use. *Ecol. Eng.* **2016**, *103*, 455–469. [[CrossRef](#)]
37. Liu, C.; Nepf, H. Sediment deposition within and around a finite patch of model vegetation over a range of channel velocity. *Water Resour. Res.* **2016**, *52*, 600–612. [[CrossRef](#)]
38. Hu, Z.H.; Lei, J.R.; Liu, C.; Nepf, H. Wake structure and sediment deposition behind models of submerged vegetation with and without flexible leaves. *Adv. Water Resour.* **2018**, *118*, 28–38. [[CrossRef](#)]
39. Lu, J.; Dai, H.C. Three dimensional numerical modeling of flows and scalar transport in a vegetated channel. *J. Hydro-Environ. Res.* **2017**, *16*, 27–33. [[CrossRef](#)]
40. Lu, J.; Dai, H.C. Numerical modeling on pollution transport in flexible vegetation. *Appl. Math. Model.* **2018**, *64*, 93–105. [[CrossRef](#)]
41. Huang, Y.H. Impact of Vegetation on the Dissipation Process of Supersaturated Total Dissolved Gas. Master's Thesis, Sichuan University, Sichuan, China, 2017. (In Chinese)
42. Huai, W.X.; Hu, Y.; Zeng, Y.H.; Han, J. Velocity distribution for open channel flows with suspended vegetation. *Adv. Water Resour.* **2012**, *49*, 56–61. [[CrossRef](#)]
43. Yang, Z.H.; Bai, F.P.; Huai, W.X.; An, R.D.; Wang, H.Y. Modelling open-channel flow with rigid vegetation based on two-dimensional shallow water equations using the lattice Boltzmann method. *Ecol. Eng.* **2017**, *106*, 75–81. [[CrossRef](#)]
44. Beudin, A.; Kalra, T.S.; Ganju, N.K.; Wamer, J.C. Development of a coupled wave-flow-vegetation interaction model. *Comput. Geosci.* **2016**, *100*, 76–86. [[CrossRef](#)]
45. Politano, M.S.; Carrica, P.M.; Turan, C.; Weber, L. A multidimensional two-phase flow model for the total dissolved gas downstream of spillways. *J. Hydraul. Res.* **2007**, *45*, 165–177. [[CrossRef](#)]
46. Politano, M.S.; Carrica, P.; Weber, L. A multiphase model for the hydrodynamics and total dissolved gas in tailraces. *Int. J. Multiph. Flow* **2009**, *35*, 1036–1050. [[CrossRef](#)]
47. Fu, X.L.; Li, D.; Zhang, X.F. Simulations of the three-dimensional total dissolved gas saturation downstream of spillways under unsteady conditions. *J. Hydrodyn.* **2010**, *22*, 598–604. [[CrossRef](#)]
48. Geldert, D.A.; Gulliver, J.S.; Wilhelms, S.C. Modeling dissolved gas supersaturation below spillway plunge pools. *J. Hydraul. Eng.* **1998**, *124*, 513–521. [[CrossRef](#)]

